



Synergistic d-p hybridized Co/W₅N₄ heterostructure catalyst for industrial alkaline water/seawater hydrogen evolution

Shipeng Geng^a, Liming Chen^a, Lianmei Kang^a, Ruchun Li^b, Haixin Chen^a, Luo Cheng^a, Dandan Cai^a, Yi Wang^{a,*}, Shuqin Song^{a,*}

^a The Key Lab of Low-carbon Chemistry & Energy Conservation of Guangdong Province, PCFM Laboratory, School of Materials Science and Engineering, School of Chemical Engineering and Technology, Sun Yat-sen University, Guangzhou 510275, PR China

^b Faculty of Chemistry and Chemical Engineering, Yunnan Normal University, Kunming 650500, PR China



ARTICLE INFO

Keywords:

Co/W₅N₄ heterostructure
d-p orbital hybridization
Industrial current density
Alkaline water/seawater electrolysis

ABSTRACT

Developing efficient and durable non-precious metal electrocatalysts with industrial current density is urgent for hydrogen evolution reaction from alkaline water/seawater but remains challenging. Here, a heterostructured Co/W₅N₄ catalyst with porous structure is innovatively constructed. The theoretical calculations confirm the strong d-p hybridization between Co and N at the interface of Co/W₅N₄ with the modulation of d-band center of Co sites. The synergistic effect between Co and W₅N₄ is disclosed that H₂O can rapidly dissociate on the W sites to generate H* adsorbed at the Co sites for favorable H₂ production. Consequently, the Co/W₅N₄ catalyst affords low overpotentials of 113 and 118 mV to drive current density of 100 mA cm⁻² in alkaline water/seawater electrolytes, respectively, which are even superior to those of commercial Pt/C. More importantly, it can also present outstanding HER stability at large current density of 500 mA cm⁻² for over two weeks (350 h) in alkaline water/seawater electrocatalysis.

1. Introduction

Hydrogen is a clean and efficient energy carrier owing to its environmentally friendly and high energy density (142 kJ g⁻¹ based on higher thermal enthalpy value), making it an ideal energy source for achieving carbon peaking and carbon neutrality goals [1–3]. Among various hydrogen production strategies, water electrolysis driven by excess renewable energy sources including wind and solar power has received great attention due to its highly economical and zero carbon emissions [4–7]. Alkaline water electrolysis is often more attractive by reason of its advantages of simple and cheap equipment and the absence of acid corrosion than the case in acidic counterpart [8–12]. To further accelerate alkaline hydrogen evolution reaction (HER), the development of efficient and stable electrocatalysts to reduce the additional kinetic energy barrier associated with the dissociation of water for industrial-grade current densities (≥ 300 mA cm⁻²) is of paramount importance [13,14]. Simultaneously, direct seawater electrocatalysis for hydrogen production has recently appealed widespread research interest attributable to its inexhaustible availability [15–17]. However, the complex composition of natural seawater can lead to the competing side

reaction and the corrosion of catalyst, and in this way reduce the efficiency of seawater electrolysis [18–20]. Therefore, there is an urgent need to develop high-performance seawater HER catalysts with high activity, low corrosivity and outstanding stability.

Recently, much effort has been devoted to the identification of effective non-precious metal catalysts as a replacement for Pt-based catalysts, which are restricted because of their high cost and scarcity [21–24]. Among them, transition metal nitrides, especially molybdenum and tungsten-based nitrides (MoN_x, WN_x), have attracted great interest due to their high electrical conductivity and excellent intrinsic catalytic activity [25–27]. However, recent experimental and theoretical studies have shown that most molybdenum/tungsten nitrides have weak water dissociation kinetics, which limits their HER performance [27]. Currently, the heterostructured construction of nitride-based catalysts can enhance water dissociation ability and thus possess considerable HER activity with respect to the state-of-the-art Pt/C. For instance, heterostructured Co/MoN nanosheet array electrocatalysts were developed on nickel foam and exhibited excellent HER activity, with an overpotential of 132 mV to drive a current density of 100 mA cm⁻² in 1.0 M KOH, possessing Pt-like catalytic performance

* Corresponding authors.

E-mail addresses: wangyi76@mail.sysu.edu.cn (Y. Wang), stsssq@mail.sysu.edu.cn (S. Song).

[28]. $\text{Mo}_2\text{C}/\text{MoN}/\text{NG}$ (NG: N-doped graphene) with highly dispersed active sites were synthesized by a novel ion-exchange method and exhibited an overpotential of 78.8 mV at 10 mA cm^{-2} in 0.5 M H_2SO_4 solution, which was about 30% less active than that of Pt/C (20 wt%) [29]. Whereas, the interactions at the interface during the electrocatalysis remain ambiguous. Simultaneously, most of the reported MoN_x and WN_x based catalysts have been mainly adopted for pure water electrocatalysis at small current densities ($< 300 \text{ mA cm}^{-2}$). For example, self-supporting tungsten nitride nanowires decorated with tungsten-cobalt alloy nanoparticles on flexible carbon cloth ($\text{Co}_3\text{W}/\text{WN}/\text{CC}$) were synthesized and exhibited a low overpotential of 43 mV and 40 h stability at 10 mA cm^{-2} in 1.0 M KOH [30]. An $\text{Ni}/\text{W}_5\text{N}_4$ Mott-Schottky heterojunction catalyst supported on NF was synthesized, showing a low overpotential of 25 mV at 10 mA cm^{-2} for HER and could be stably operated for 100 h at both 10 and 100 mA cm^{-2} [31]. Whereas, the above catalysts do not meet the requirements for stable HER at industrial current densities. Therefore, it is of great interest and challenge to design ideal heterostructured nitride-based catalysts for industrial-scale, high current density and stable alkaline water/seawater HER and further elaborate their underlying catalytic mechanism at the interface.

Here, we design a unique $\text{Co}/\text{W}_5\text{N}_4$ heterostructure catalyst with distinct synergistic effects on the efficient and robust alkaline water/seawater electrocatalysis. The obtained $\text{Co}/\text{W}_5\text{N}_4$ possesses a porous surface derived from ammonia reduction treatments, which can expose abundant active sites and provide rich heterogeneous interfaces for HER. Theoretical calculations confirm that the apparent d-p orbital hybridization between the Co and N atom in $\text{Co}/\text{W}_5\text{N}_4$ not only accelerates the dissociation of H_2O , but also decreases the d-band center of Co, which facilitates the adsorption and desorption of the H intermediate. As a result, the optimum $\text{Co}/\text{W}_5\text{N}_4$ catalyst exhibits excellent HER performance and high stability. In addition, with the obtained $\text{Co}/\text{W}_5\text{N}_4$ catalyst and the NiFe layered double hydroxide (NiFe-LDH) as the respective cathode and anode catalysts, the $\text{Co}/\text{W}_5\text{N}_4||\text{NiFe-LDH}$ pair shows superior overall water/seawater electrocatalytic activity and stability, demonstrating great potential for practical application.

2. Experimental

2.1. Materials

All materials below were of analytical grade and directly used unless otherwise stated. Ammonium metatungstate ($(\text{NH}_4)_6\text{H}_2\text{W}_{12}\text{O}_{40} \cdot x\text{H}_2\text{O}$) and cobalt nitrate ($\text{Co}(\text{NO}_3)_2 \cdot 6\text{H}_2\text{O}$) were purchased from Aladdin Corporation (Shanghai, China). Nickel foam (NF) was purchased from LiGe Technology Ltd. (Guangzhou, China). Analytical grade $\text{C}_2\text{H}_5\text{OH}$ and HCl were purchased from Guangzhou Chemical Reagent Factory (Guangzhou, China). Deionized (DI) water was sourced from the chemistry laboratory center of Sun Yat-sen University.

2.2. Catalysts preparation

Firstly, the NF was cleaned with 3.0 M HCl aqueous solution, DI water and ethanol, each step being sonicated for 10 min to remove the oxide layer from the NF surface. Next, a piece of treated NF (3.5 cm \times 5.0 cm) was vertically placed in a 100 mL Teflon lined stainless autoclave, followed by the addition of 60.0 mL of a homogeneous solution containing 0.25 mmol of $(\text{NH}_4)_6\text{H}_2\text{W}_{12}\text{O}_{40} \cdot x\text{H}_2\text{O}$ and 3.00 mmol of $\text{Co}(\text{NO}_3)_2 \cdot 6\text{H}_2\text{O}$. The Teflon lined stainless autoclave was then sealed and heated at 180 °C for 10 h. After natural cooling down to room temperature, the $\text{Co}_4\text{W}_6\text{O}_{21}(\text{OH})_2 \cdot 4\text{H}_2\text{O}$ precursor was grown on NF. To obtain $\text{Co}/\text{W}_5\text{N}_4$, the prepared $\text{Co}_4\text{W}_6\text{O}_{21}(\text{OH})_2 \cdot 4\text{H}_2\text{O}$ were treated at different temperatures of 400, 500 and 600 °C for 2 h in NH_3 atmosphere with a heating rate of 10 °C min^{-1} for nitridation. The corresponding samples were denoted as $\text{Co}/\text{W}_5\text{N}_4-x$ ($x = 400, 500$ and 600). Meanwhile, the W_5N_4 catalyst was prepared under the same conditions except that Co

$(\text{NO}_3)_2 \cdot 6\text{H}_2\text{O}$ was not added during the hydrothermal process. A NiFe-LDH on NF was prepared according to the reported literature [32], which was used as an oxygen evolution reaction (OER) catalyst to couple with $\text{Co}/\text{W}_5\text{N}_4$ for overall water electrolysis. Briefly, 1.2 mmol Ni $(\text{NO}_3)_2 \cdot 6\text{H}_2\text{O}$, 0.4 mmol $\text{Fe}(\text{NO}_3)_3 \cdot 9\text{H}_2\text{O}$, 4.0 mmol NH_4F and 20.0 mmol urea were homogeneously dissolved in 60.0 mL DI water in a beaker. A piece of NF was placed inside the beaker and then underwent a hydrothermal reaction at 90 °C for 8 h. The product was denoted as Ni-Fe LDH.

2.3. Theoretical calculations

Density functional theory (DFT) calculations were carried out using the Vienna ab initio simulation package (VASP) based on first principles [33]. The projector augmented wave (PAW) method [34] and Perdew-Burke-Ernzerhof (PBE) [35] exchange-correlation functional were implemented. Spin polarization was taken into consideration. Van der Waals interactions were corrected by the DFT-D3 method. A vacuum space of 15 Å was used to prevent the interaction between adjacent layers. All calculations were performed at a cut-off energy of 400 eV. In addition, 10⁻⁶ eV and 0.05 eV Å⁻¹ were used for convergence criteria for energy and force. The adsorption energy (E_{ads}) of species X can be given by Eq. (1):

$$E_{\text{ads}} = E(\text{X/slab}) - E(\text{X}) - E(\text{slab}) \quad (1)$$

where a more negative E_{ads} implies stronger adsorption. The Gibbs free energy (ΔG) of the adsorbate can be calculated by Eq. (2):

$$\Delta G = \Delta E + \Delta ZPE - T\Delta S \quad (2)$$

where ΔE is the electron energy (eV), T is the absolute temperature (298.15 K), ΔZPE and ΔS are the change in zero-point energy (eV) and entropy (J mol⁻¹ K⁻¹), and they can be calculated in terms of vibrational frequency. To measure the energy barrier for water dissociation, the transition state (TS) was determined using the elastic band nudged-climbing image (CI-NEB) approach [36].

3. Result and discussion

3.1. Structural characterization

As illustrated in Fig. 1a, a self-supporting $\text{Co}_4\text{W}_6\text{O}_{21}(\text{OH})_2 \cdot 4\text{H}_2\text{O}$ polyhedra precursor was first grown on NF by a hydrothermal reaction, and then converted into a $\text{Co}/\text{W}_5\text{N}_4$ by high-temperature nitridation under an NH_3 atmosphere. The photos in Fig. S1a-c show an obvious color change from silver on pure NF, then purple of precursors and finally black in $\text{Co}/\text{W}_5\text{N}_4$ case. XRD was used to study the crystal structure of the prepared samples. As shown in Fig. 1b, the characteristic peaks of the precursor powder perfectly correspond to the cubic $\text{Co}_4\text{W}_6\text{O}_{21}(\text{OH})_2 \cdot 4\text{H}_2\text{O}$ (PDF #47-0142) [37]. After high-temperature nitridation treatment, the XRD patterns of the powder sample can be defined as W_5N_4 (PDF #65-4761) and Co (PDF #01-2930), demonstrating the successful synthesis of the heterostructured $\text{Co}/\text{W}_5\text{N}_4$ catalyst. The XRD results in Fig. S2 also indicate the successful preparation of W_5N_4 and $\text{Co}/\text{W}_5\text{N}_4$ on NF. Noted that the XRD peaks of metallic Co can not be observed due to the interference of NF substrate. Moreover, SEM images (Fig. 1c and S3a-b) show that the precursors with the smooth regular polyhedral shape can be uniformly grown on NF surface. The energy dispersive spectroscopy (EDS) mapping images (Fig. S3c-f) present that Co, W and O elements are evenly distributed. On the one hand, after nitridation, the $\text{Co}/\text{W}_5\text{N}_4$ still retains the polyhedra morphology (Fig. 1d and S4a-c). On the other hand, due to the etching effect of NH_3 at high-temperature condition, a unique porous structure is generated. The high-resolution SEM image in Fig. S4a shows the abundant porous structure on the polyhedra surface, which can facilitate the transport of electrolyte during electrocatalysis and expose catalytically active sites [38]. In addition, to determine the detailed composition of the

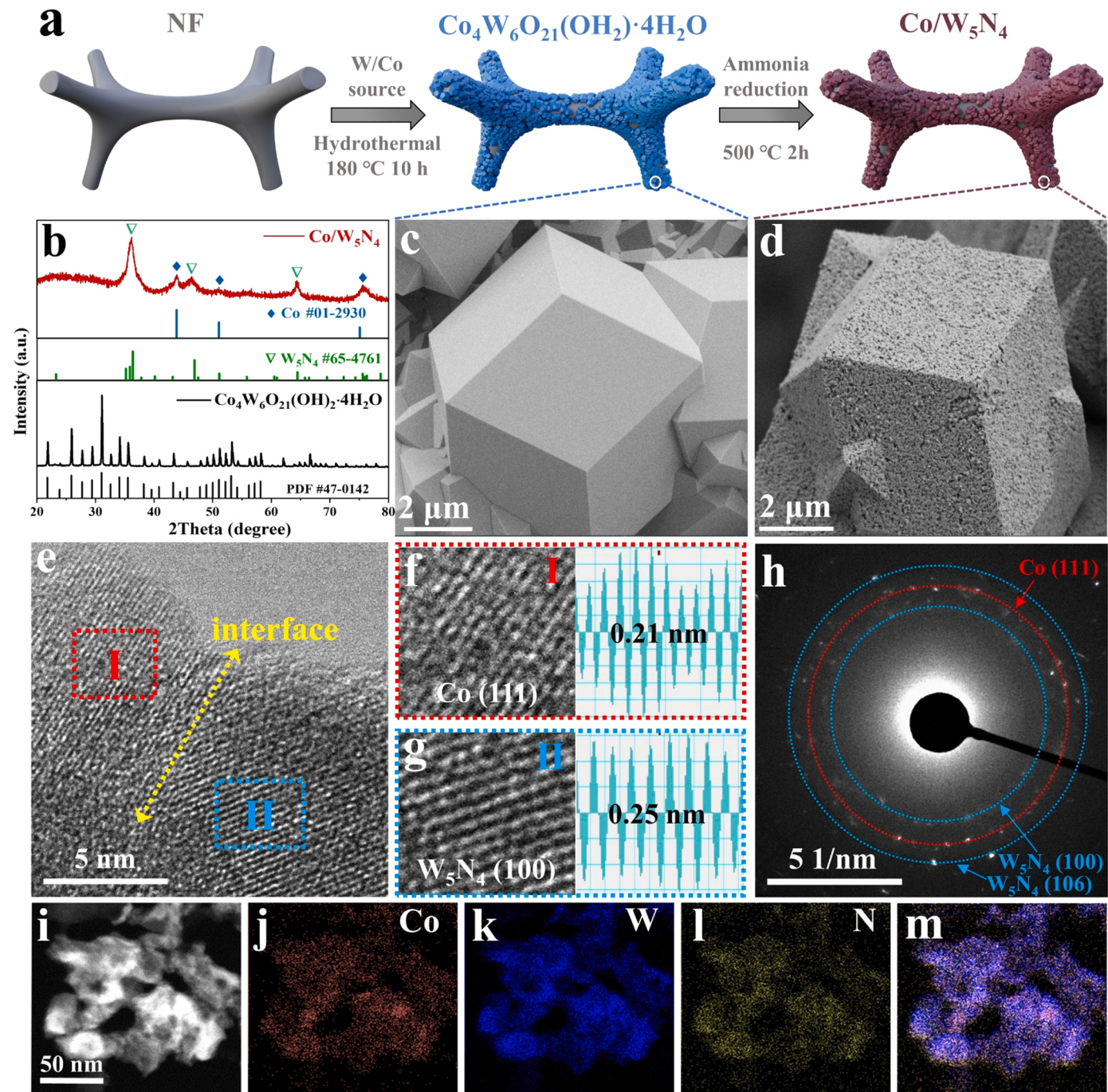


Fig. 1. (a) Schematic flow diagram for the synthesis of $\text{Co}/\text{W}_5\text{N}_4$. (b) XRD patterns from the powders of $\text{Co}_4\text{W}_6\text{O}_{21}(\text{OH})_2\cdot 4\text{H}_2\text{O}$ precursor and $\text{Co}/\text{W}_5\text{N}_4$. (c) SEM image of $\text{Co}_4\text{W}_6\text{O}_{21}(\text{OH})_2\cdot 4\text{H}_2\text{O}$ precursor. (d) SEM, (e-g) HRTEM and (h) SAED images of $\text{Co}/\text{W}_5\text{N}_4$. (i-m) TEM elemental mapping images of Co, W, N and overlapped Co, W and N for $\text{Co}/\text{W}_5\text{N}_4$.

$\text{Co}/\text{W}_5\text{N}_4$, the high-resolution TEM (HRTEM), selected area electron diffraction (SAED) and EDS characterizations were employed. The HRTEM image in Fig. 1e reveals clear lattice spacing of 0.21 (Fig. 1f) and 0.25 nm (Fig. 1g), consistent with that of the (111) facet of metallic Co and the (100) facet of W_5N_4 , respectively. These results demonstrate the heterostructure formation of the $\text{Co}/\text{W}_5\text{N}_4$. Simultaneously, the SAED pattern in Fig. 1h also presents the polycrystalline rings of both metallic Co (111) and W_5N_4 (100) and (106), further indicating the interface structure in the $\text{Co}/\text{W}_5\text{N}_4$. The EDS mapping images (Fig. 1i-m) prove the uniform distribution of Co, W and N elements in $\text{Co}/\text{W}_5\text{N}_4$.

Different nitriding treatment temperatures often have a significant influence on material morphology and performance. Fig. S5a exhibits

the XRD patterns of the samples obtained at different treatment temperatures. The diffraction peaks of cobalt tungstate oxide CoWO_4 , which may be the intermediate state in the high-temperature reduction process, still appear at the low heating temperature of 400 °C, implying the incomplete nitridation. The perfect $\text{Co}/\text{W}_5\text{N}_4$ heterostructure can be formed at the heating temperature of 500–600 °C. However, small nanoparticles can be observed on the material surface when the calcination temperature is 600 °C (Fig. S5c), which could be due to the material collapse and agglomeration caused by the high temperature treatment. Accordingly, it can be concluded that the optimum synthetic temperature for the $\text{Co}/\text{W}_5\text{N}_4$ heterostructure is 500 °C. Furthermore, the SEM images in Fig. S6a-b indicate that W_5N_4 possesses a spindle-

shaped morphology and the lattice distance of 0.25 nm obtained by HRTEM (Fig. S6c) corresponds to the (100) facet of W_5N_4 , indicating the successful formation of W_5N_4 .

To investigate the chemical state of the surface elements of as-prepared catalysts, XPS was employed. As displayed in Fig. S7, the peak intensity of the N 1 s in the XPS spectra of W_5N_4 and Co/ W_5N_4 is significantly stronger than that of the $Co_4W_6O_{21}(OH)_2\cdot4H_2O$ precursor due to the generation of nitrides. The high-resolution Co XPS spectrum of the $Co_4W_6O_{21}(OH)_2\cdot4H_2O$ precursor (Fig. 2a) shows two peaks at 781.5 and 797.7 eV, which are allocatable to the Co^{2+} species in the Co-O bond. For the Co 2p XPS spectrum of Co/ W_5N_4 catalyst, two new peaks at 778.6 and 793.7 eV are observed [28], corresponding to the metallic Co obtained during nitridation. Moreover, the high-resolution XPS spectra of W 4 f are shown in Fig. 2b. It can be seen that two peaks at 37.7 and 35.6 eV in the $Co_4W_6O_{21}(OH)_2\cdot4H_2O$ precursor exist, being allocated to W 4 $f_{5/2}$ and W 4 $f_{7/2}$ from the W-O bond. After nitridation treatment, the W 4 f spectra of W_5N_4 and Co/ W_5N_4 have two foreign peaks at ~ 33.4 (W 4 $f_{7/2}$) and ~ 35.6 eV (W 4 $f_{5/2}$), corresponding to the signal peaks of the W-N bond, indicating the successful formation of W_5N_4 during the nitridation treatment. Besides, as shown in Fig. 2c, for Co/ W_5N_4 , the XPS peak at 397.7 eV of N 1 s is assigned to the W-N bond, while the characteristic peaks at 399.8 and 401.0 eV should be attributed to the N-H group and N-O species, respectively [31]. It is noteworthy that both W 4 f and N 1 s signal peaks in the W-N bond for Co/ W_5N_4 show a significant negative shift (~ 0.2 eV) compared with those of W_5N_4 (Fig. 2b and c), which can be stemmed from the strong electron transfer from the metallic Co phase to the W_5N_4 phase at the interface of Co/ W_5N_4 [31].

3.2. Electrocatalytic performance

The HER performance of the catalysts was first evaluated using a standard three-electrode setup in a 1.0 M KOH alkaline aqueous solution. According to the linear sweep voltammetry (LSV) curves in Fig. 3a, the Co/ W_5N_4 catalyst only needs low overpotentials (η) of 30 and 113 mV for achieving current densities of 10 and 100 $mA\ cm^{-2}$, respectively. These performances are superior to the corresponding values of the NF (225 and 368 mV), $Co_4W_6O_{21}(OH)_2\cdot4H_2O$ precursor (196 and 392 mV) and W_5N_4 (43 and 223 mV), whereas similar to those of the benchmark Pt/C (25 and 123 mV). Moreover, Co/ W_5N_4 requires a low overpotential of 227 mV to achieve an industrial current density of 500 $mA\ cm^{-2}$, which is superior to that of Pt/C (330 mV). Furthermore, to investigate the kinetics of the HER, the Tafel slope of the catalyst was determined from the LSV curve. As displayed in Fig. 3b, the Tafel slope of Co/ W_5N_4 , NF, $Co_4W_6O_{21}(OH)_2\cdot4H_2O$ precursor and W_5N_4 is 91.8, 103, 153.4 and 162.9 $mV\ dec^{-1}$, respectively, indicating the Volmer-Heyrovsky mechanism for all samples [39]. Among them, the lowest Tafel slope of Co/ W_5N_4 confirms the most favorable catalytic kinetics. Furthermore, the excellent activity of Co/ W_5N_4 surpasses the majority of

nitride-based catalysts and others reported previously (Fig. 3c and Table S1).

The electrochemical impedance spectroscopy (EIS) and electrochemically active surface area (ECSA) were applied to reveal the intrinsic properties of the catalyst. First, the fitted Nyquist plot (Fig. S8) reveals that Co/ W_5N_4 has the smallest charge transfer resistance (R_{ct}) of approximate $2.2\ \Omega$ significantly less than $Co_4W_6O_{21}(OH)_2\cdot4H_2O$ precursor ($\sim 184\ \Omega$) and W_5N_4 ($\sim 39\ \Omega$). The much smaller R_{ct} of Co/ W_5N_4 can be contributed to the introduction of the metallic Co, implying faster electron transfer capability. Moreover, it is known that the ECSA of the catalyst is positively correlated with the electrochemical double-layer capacitance (C_{dl}) [40]. Cyclic voltammetric curves (CVs) at different scan rates were obtained to calculate the C_{dl} (Fig. S9). As shown in Fig. 3d, benefiting from the porous structure, the Co/ W_5N_4 exhibits a high C_{dl} value of $170.6\ mF\ cm^{-2}$, which is much larger than that of NF ($1.1\ mF\ cm^{-2}$), the $Co_4W_6O_{21}(OH)_2\cdot4H_2O$ precursor ($3.5\ mF\ cm^{-2}$) and W_5N_4 ($43.2\ mF\ cm^{-2}$). These results reveal that the construction of metallic Co and porous microstructure of Co/ W_5N_4 by controlled nitridation treatment is favorable for improving the catalyst conductivity and increasing catalytic active sites, which greatly enhances the HER performance. Furthermore, Fig. S10 shows the LSV curves and EIS plots of catalysts annealed at different temperatures of 400, 500 and 600 $^{\circ}C$. Obviously, the Co/ W_5N_4 -500 exhibits an optimal HER performance and R_{ct} value. The lower performance of Co/ W_5N_4 -400 may be caused by the incomplete nitridation. While Co/ W_5N_4 -600 also delivers a low HER performance probably due to the material collapse and agglomeration as previously described in Fig. S5.

Due to the inexhaustible availability, direct seawater electrocatalysis has recently attracted considerable attention. The HER performance of prepared catalysts was also evaluated in a simulated seawater environment (1.0 M KOH + 0.5 M NaCl) to extend their possible applications. As displayed in Fig. 3e, the Co/ W_5N_4 still exhibits optimal catalytic performance and only requires overpotentials of 118 and 273 mV to obtain current densities of 100 and 500 $mA\ cm^{-2}$, respectively. This outstanding HER catalytic activity outperforms that of the Pt/C. Given that NaCl concentration increases with continuous water consumption in the seawater catalytic process, the Co/ W_5N_4 catalyst performance in a harsher chlorine environment was evaluated to verify its resistance to corrosive chlorine ions. From Fig. S11, it can be seen that there is no obvious performance change in 1.0 M KOH + 1.0 M NaCl and 1.0 M KOH + 2.0 M NaCl electrolytes, with only a slight decrease in the performance compared with that in 1.0 M KOH + 0.5 M NaCl, which proves its excellent chlorine tolerance. Generally, in industrial applications, catalyst stability is considered as a critical parameter. To evaluate the durability of the Co/ W_5N_4 catalyst, CV potential cycles were first tested. After 10,000 (10k) CVs cycles in a potential range from 0 to $-0.17\ V$ (vs. RHE) under alkaline water/seawater conditions for the Co/ W_5N_4 catalyst, the LSV curve only has a little decline at large current densities compared with the initial case (Fig. 3f). Fig. 3g shows the

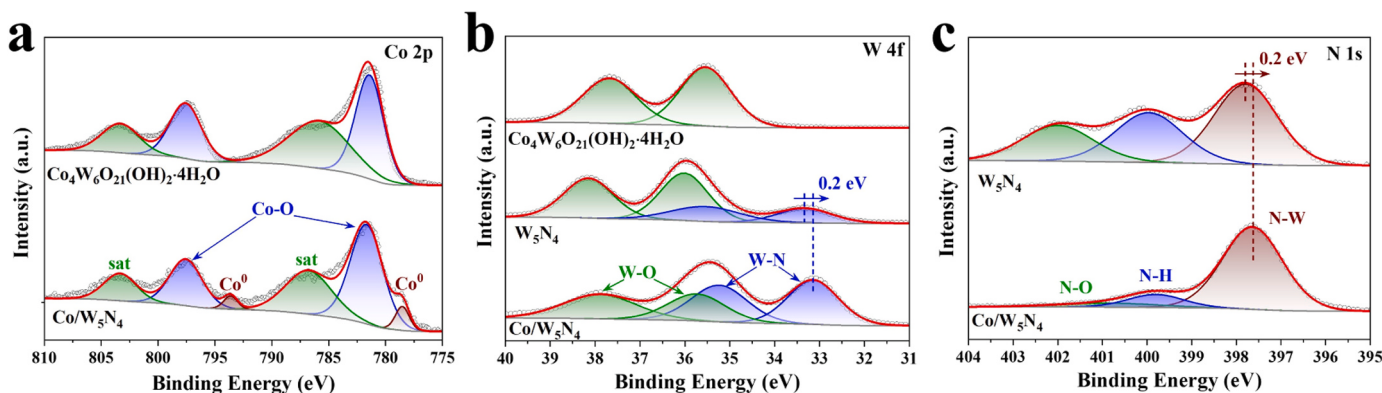


Fig. 2. High-resolution XPS spectra of (a) Co 2p, (b) W 4 f and (c) N 1 s for Co/ W_5N_4 catalyst and contrast samples.

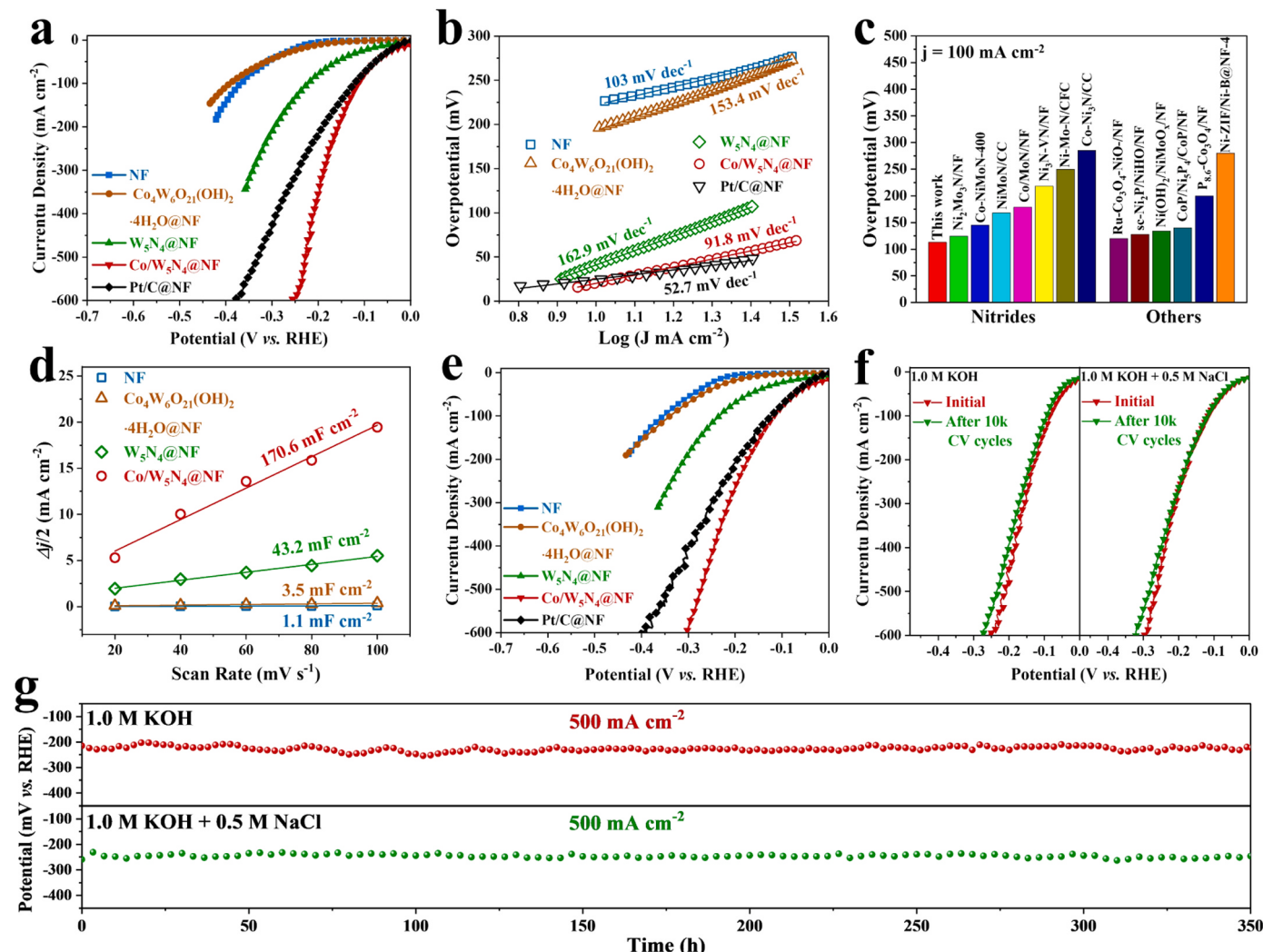


Fig. 3. (a) LSV curves and (b) corresponding Tafel plots of NF, $\text{Co}_4\text{W}_6\text{O}_{21}(\text{OH})_2 \cdot 4\text{H}_2\text{O}$ precursor, W_5N_4 and $\text{Co}/\text{W}_5\text{N}_4$ catalysts in 1.0 M KOH electrolyte. (c) HER performance comparison between $\text{Co}/\text{W}_5\text{N}_4$ and recently reported catalysts. (d) C_{dl} values of as-prepared catalysts. (e) LSV curves of the as-prepared catalysts in $1.0 \text{ M KOH} + 0.5 \text{ M NaCl}$ electrolyte. (f) LSV curves before and after CV cycling and (g) chronopotentiometric curves of $\text{Co}/\text{W}_5\text{N}_4$.

chronopotentiometric curve at 500 mA cm^{-2} of the $\text{Co}/\text{W}_5\text{N}_4$ catalyst in 1.0 M KOH and $1.0 \text{ M KOH} + 0.5 \text{ M NaCl}$ electrolytes. There is no significant performance degradation observed on the $\text{Co}/\text{W}_5\text{N}_4$ catalyst even after a continuous test of 350 h (over two weeks). We further explored the composition and morphology of the $\text{Co}/\text{W}_5\text{N}_4$ catalysts after prolonged HER catalytic stability testing in $1.0 \text{ M KOH} + 0.5 \text{ M NaCl}$. As clearly seen from Fig. S12a, after the stability test, the $\text{Co}/\text{W}_5\text{N}_4$ catalyst has the similar XRD patterns similar to the initial one. The SEM image (Fig. S12b) indicates no visible change in the overall morphology of the $\text{Co}/\text{W}_5\text{N}_4$ catalyst. High resolution Co XPS spectra (Fig. S13a) after stability tests indicate the disappearance of zero-valent Co and the appearance of high-valent Co^{3+} , possibly originating from CoOOH , which has been widely reported [41,42]. In contrast, the fine XPS spectra of W 4f and N 1s (Fig. S13b and c) have no clear change with respect to the initial state, indicating the stability of W_5N_4 in the high-current stability test. These results demonstrate the excellent structure stability of $\text{Co}/\text{W}_5\text{N}_4$ catalyst at high current densities, suggesting a remarkable potential for application in industrial alkaline water/seawater electrolysis. Furthermore, the raw seawater was collected to evaluate the performance and stability of $\text{Co}/\text{W}_5\text{N}_4$ catalyst. Fig. S14a shows the preparation of $1.0 \text{ M KOH} +$ seawater with large amounts of insoluble white precipitates ($\text{Ca}(\text{OH})_2$ and $\text{Mg}(\text{OH})_2$). Then the supernatant was extracted for subsequent electrochemical test.

Fig. S14b indicates that the performance of $\text{Co}/\text{W}_5\text{N}_4$ in $1.0 \text{ M KOH} +$ seawater requires low overpotentials of 117 and 292 mV to reach 100 and 500 mA cm^{-2} , which is only slightly worse than that in $1.0 \text{ M KOH} + 0.5 \text{ M NaCl}$ electrolyte. Moreover, the $\text{Co}/\text{W}_5\text{N}_4$ catalyst shows only about 40 mV potential fluctuations after 50 h stability test at an industrial current density of 500 mA cm^{-2} , as displayed in Fig. S14c. These results indicate that the $\text{Co}/\text{W}_5\text{N}_4$ catalyst still shows excellent performance and stability under actual alkaline seawater conditions.

3.3. Mechanism analysis

In order to elucidate the mechanism of the $\text{Co}/\text{W}_5\text{N}_4$ catalyst for efficient HER, the density functional theory (DFT) calculations were performed. Firstly, the W in the W_5N_4 unit cell is fractionally occupied. To efficiently conduct DFT calculations, one W atom in the unit cell is removed to reach chemical equilibrium. This causes the unit cell to restructure with the generation of the specific Z-axis-orientated stresses, as shown in Fig. S15a. After optimizing the Z-axis length, the lowest energy of 17.1 \AA is selected as the final W_5N_4 unit cell model for the subsequent calculations (Fig. S15b). Fig. 4a shows a typical model of $\text{Co}/\text{W}_5\text{N}_4$ heterostructure, which is built based on the previous experimental results. The $\text{W}_5\text{N}_4(100)$ and metallic $\text{Co}(111)$ model are also constructed as shown in Fig. S16. The charge density difference (Fig. 4b,c) exhibits a

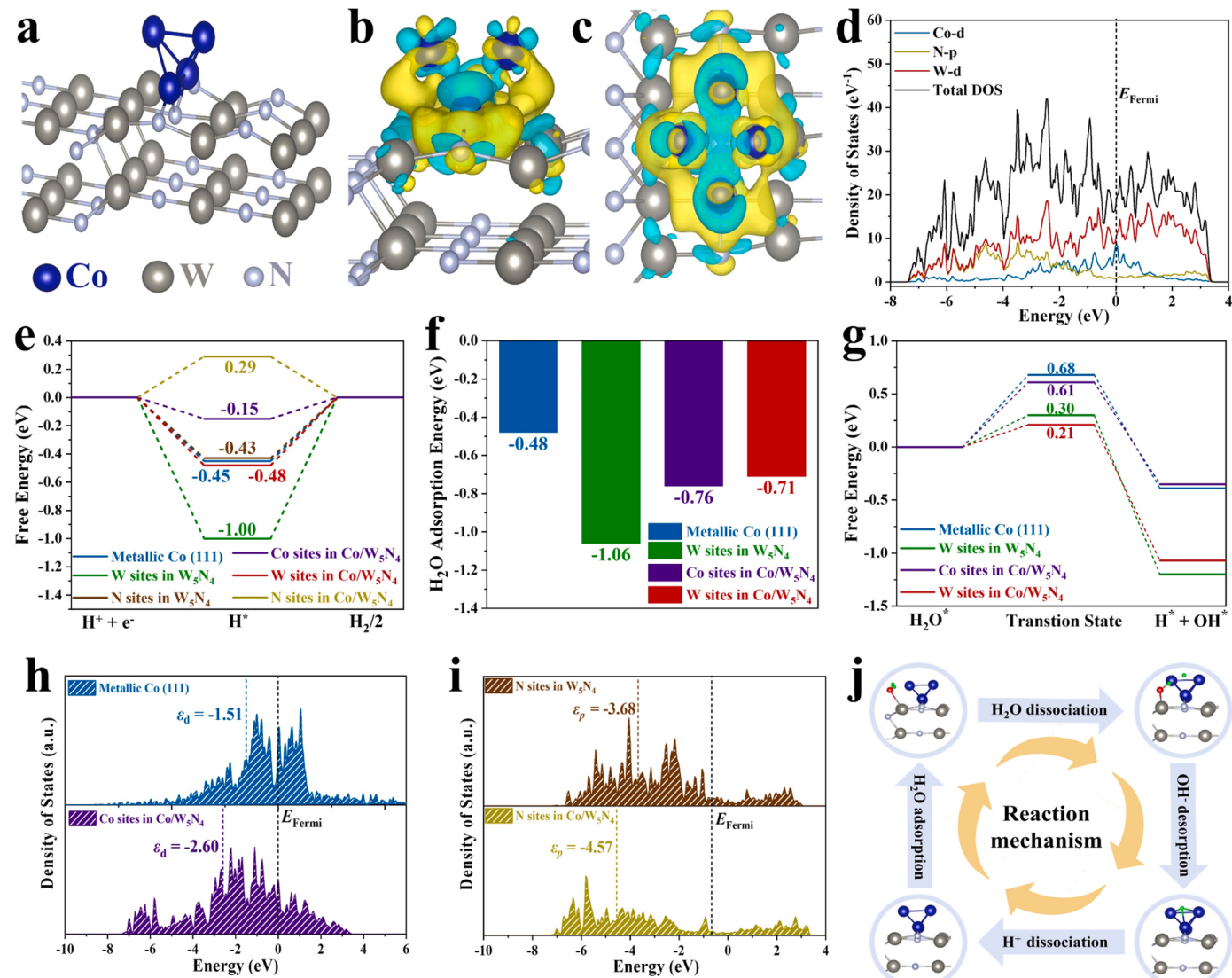


Fig. 4. (a) Co/W₅N₄ model for DFT calculations. (b) Side and (c) top views of charge density differences in Co/W₅N₄. Electron accumulation and depletion are indicated by the yellow and cyan regions, respectively. (d) DOS calculated for total Co, W and N in Co/W₅N₄. Fermi level is shown by black dashed line. (e) ΔG_{H^*} for metallic Co(111), W and N sites in W₅N₄(100), and Co, W and N sites in Co/W₅N₄. (f) $E_{ads}(H_2O)$ and (g) $\Delta G_{dis}(H_2O)$ for metallic Co(111), W sites in W₅N₄(100) and Co, W sites in Co/W₅N₄. (h) DOS calculated for Co sites in Co(111) and Co/W₅N₄ heterogeneous interface. (i) DOS calculated for N sites in W₅N₄(100) and Co/W₅N₄ heterogeneous interface. (j) HER reaction pathway diagram for Co/W₅N₄.

significant charge accumulation at the heterogeneous interface of the Co/W₅N₄ catalysts, especially between Co and Co-coordinated N sites. This suggests that an obvious d-p hybridization between Co and N atoms in Co/W₅N₄ is induced, thus providing a strong charge exchange and electronic modulation [43,44]. Meanwhile, the obvious orbital occupation on the Fermi energy level in the total density of states (DOS) (Fig. 4d) indicates the metallic feature of Co/W₅N₄ catalyst with excellent conductivity, which is consistent with the EIS results [45].

According to the Tafel slope (91.8 mV dec⁻¹), the HER process of Co/W₅N₄ follows the Volmer-Heyrovsky pathway. The H₂O adsorption energy, the energy barrier for H₂O dissociation and the H adsorption energy were subsequently calculated to investigate the HER mechanism of the Co/W₅N₄ catalyst. The H adsorption energy (ΔG_{H^*}) was calculated first. The Co, W and N sites of Co/W₅N₄, the W and N sites of W₅N₄(100) and the Co site of Co(111) were considered as active sites, and the corresponding H adsorption structures are shown in Fig. S17. As shown in Fig. 4e, it can be seen that a small ΔG_{H^*} for the W (-1.00 eV) and N (-0.43 eV) sites in W₅N₄(100) and Co (-0.45 eV) sites in Co(111) indicates that they are easy to adsorb H, but the desorption of H

intermediates is sluggish. In contrast, the ΔG_{H^*} value of the Co, W and N sites in Co/W₅N₄ is -0.15, -0.48 and 0.29 eV, respectively, which is effectively optimized relative to the Co sites in metallic Co (-0.45 eV) and W/N sites of W₅N₄ (-1.00/-0.43 eV). The optimized ΔG_{H^*} for Co/W₅N₄ can be due to the electronic structure modulation caused by the d-p hybridization of Co and N atoms at the interface [9,45,46]. More importantly, the Co site in Co/W₅N₄ exhibits the lowest absolute value of ΔG_{H^*} (-0.15 eV), indicating that the Co sites with the most excellent H adsorption and desorption ability are the catalytically active sites for H intermediates in Co/W₅N₄. Under alkaline conditions, the HER performance of many catalysts, including Pt, is governed by the Volmer (H₂O dissociation) reaction [47,48]. Therefore, the H₂O adsorption energies ($E_{ads}(H_2O)$) and the dissociation energy barrier of H₂O ($\Delta G_{dis}(H_2O)$) were further explored. The corresponding structures of the reaction pathway for H₂O adsorption and dissociation are given in Figs. S18-20. Fig. 4f shows that the W sites of W₅N₄ possess the strongest $E_{ads}(H_2O)$ of -1.06 eV, while the Co sites Co(111) have the weakest $E_{ads}(H_2O)$ of -0.48 eV. By the construction of Co/W₅N₄, the Co and W sites in Co/W₅N₄ have moderate $E_{ads}(H_2O)$ of -0.76 and -0.71 eV. In

addition, Fig. 4g is the calculated $\Delta G_{\text{dis}}(\text{H}_2\text{O})$ and it can be seen that the Co(111) has the largest $\Delta G_{\text{dis}}(\text{H}_2\text{O})$ of 0.68 eV. A small $\Delta G_{\text{dis}}(\text{H}_2\text{O})$ of 0.30 eV can be observed on the W site in W_5N_4 , which allows for efficient adsorption (Fig. 4f) and dissociation of H_2O . However, the strong H adsorption (Fig. 4e) in W_5N_4 limits the subsequent desorption of H, and thus leads to a low catalytic HER activity. When the metallic Co is introduced, the $\Delta G_{\text{dis}}(\text{H}_2\text{O})$ of the W site and Co site for $\text{Co}/\text{W}_5\text{N}_4$ is 0.21 and 0.61 eV, respectively, implying that the W sites for $\text{Co}/\text{W}_5\text{N}_4$ can act as the active sites for the most favorable dissociation of H_2O .

To illustrate the interactions of the atoms at the $\text{Co}/\text{W}_5\text{N}_4$ heterostructure interface, we have performed electronic structure calculations for Co and the N coordinated to it. As shown in Fig. 4h, the DOS of Co in Co(111) shows its *d*-band center (ε_d) is at -1.51 eV, whereas the ε_d of Co atoms coordinated to N at the $\text{Co}/\text{W}_5\text{N}_4$ heterostructure interface is lowered to -2.60 eV. Meanwhile, the electron depletion or accumulation of the four Co atoms in $\text{Co}/\text{W}_5\text{N}_4$ from the Bader charge analysis (Fig. S21) are -0.14 , $+0.01$, $+0.13$ and $+0.11$ e, respectively. The small changes in valence electrons indicate that they are all proximate to the zero-valence state. Notably, the two Co atoms coordinated to N present a greater electron depletion ($+0.13$ and $+0.11$ e) due to the bonding effect of *d*-*p* hybridization between Co and N, resulting in a higher electron loss. The lower ε_d and fewer electrons will significantly reduce the adsorption of H, and thus bring an efficient ΔG_{H^*} (-0.15 eV) close to 0 (Fig. 4e) [44,48]. Similarly, Fig. 4i reveals that the *p*-band center of the N site coordinated to Co at the $\text{Co}/\text{W}_5\text{N}_4$ interface is significantly lowered to -4.57 eV compared with the N site of W_5N_4 (-3.68 eV). Catalyst durability is often correlated with structural stability. Therefore, the binding energy of $\text{Co}/\text{W}_5\text{N}_4$ was calculated according to Eq. (3).

$$\text{E(b)} = \text{E}(\text{Co}/\text{W}_5\text{N}_4) - \text{E}(\text{Co}) - \text{E}(\text{W}_5\text{N}_4) \quad (3)$$

The calculated very negative binding energy of -11.9 eV indicates that Co and W_5N_4 in the heterostructure can be tightly bound together and quite stable. These results show that the strong *d*-*p* hybridization between Co and N significantly modulates electronic structures for more

favorable and stable HER electrocatalysis. Ultimately, the reaction pathway of alkaline HER in the heterostructure of $\text{Co}/\text{W}_5\text{N}_4$ is revealed in Fig. 4j, where H_2O is adsorbed and dissociated on the W site of W_5N_4 and then the generated H^* is adsorbed on the Co site for the detachment of H_2 .

3.4. Overall water electrolysis performance

Given the excellent performance of $\text{Co}/\text{W}_5\text{N}_4$ heterostructured catalysts for alkaline water/seawater electrocatalysis for hydrogen production, a two-electrode cell using $\text{Co}/\text{W}_5\text{N}_4$ as the cathode and NiFe-LDH as the anode ($\text{Co}/\text{W}_5\text{N}_4||\text{NiFe-LDH}$) was designed to evaluate the overall performance of water electrolysis under alkaline water/seawater. The NiFe-LDH has been reported to exhibit excellent OER performance and chlorine resistance [49,50]. The successful preparation of flaky NiFe-LDH on NF is demonstrated by the XRD patterns and SEM images (Fig. S22). The LSV curves display that the obtained NiFe-LDH only requires 190 and 255 mV to achieve current densities of 10 and 100 mA cm^{-2} in 1.0 M KOH (Fig. S23), which verifies an attractive OER performance and is in general agreement with those reported results [47].

Fig. 5a illustrates that, to achieve 100 and 300 mA cm^{-2} at room temperature in 1.0 M KOH, the $\text{Co}/\text{W}_5\text{N}_4||\text{NiFe-LDH}$ cell only requires operational voltages of 1.63 and 1.88 V. Interestingly, the water splitting performance has no obvious change in the simulated seawater (1.0 M KOH + 0.5 M NaCl). Meanwhile, under simulated industrial conditions (6.0 M KOH or 6.0 M KOH + 0.5 M NaCl electrolyte at 60°C), the $\text{Co}/\text{W}_5\text{N}_4||\text{NiFe-LDH}$ cell exhibits a desirable property, which only needs the respective operated voltage of about 1.52, 1.63 and 1.73 V to obtain 100, 300 and 500 mA cm^{-2} current densities (Fig. 5a,b). The Faraday efficiency (FE) of hydrogen production was measured by utilizing a typical draining method at a constant current density of 100 mA cm^{-2} under 1.0 M KOH + 0.5 M NaCl condition. Fig. S24 shows photos of the electrolyzer and the H_2 yield at various

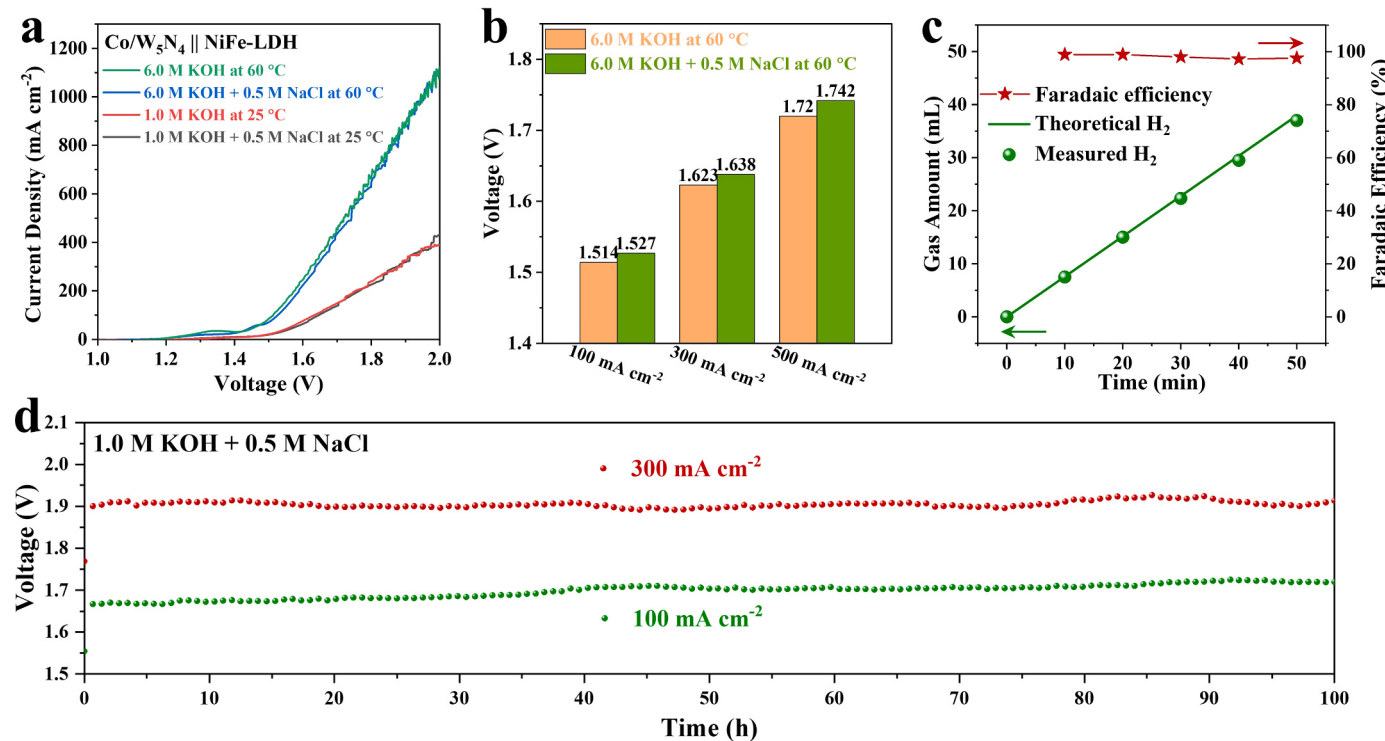


Fig. 5. (a) Overall water/seawater electrolysis performance of $\text{Co}/\text{W}_5\text{N}_4||\text{NiFe-LDH}$ pair in different electrolytes. (b) Potential required for the $\text{Co}/\text{W}_5\text{N}_4||\text{NiFe-LDH}$ pair to achieve different current densities in simulated industrial conditions. (c) Measured and theoretical gases and corresponding Faradaic efficiency from the $\text{Co}/\text{W}_5\text{N}_4$ HER in 1.0 M KOH + 0.5 M NaCl electrolyte. (d) Chronopotentiometric curves of the $\text{Co}/\text{W}_5\text{N}_4||\text{NiFe-LDH}$ pair for overall seawater electrolysis.

times. The measured amount of gas agrees with the theoretical prediction as shown in Fig. 5c, suggesting that the FE is almost 100% for hydrogen production. Besides, Fig. 5d displays the long-time stability for the Co/W₅N₄||NiFe-LDH cell at constant currents of 100 and 300 mA cm⁻² under the 1.0 M KOH + 0.5 M NaCl condition at room temperature. The negligible potential increase after 100 h stability test at both 100 and 300 mA cm⁻² proves the excellent durability of Co/W₅N₄ heterostructure catalyst for seawater electrolysis at industrial scale high current densities. The attractive catalytic activity and high stability imply the desirable potential for industrial scale water/seawater electrolysis.

In summary, Co/W₅N₄ exhibits excellent catalytic properties. Furthermore, it has advantages in terms of composite cost and environmental footprint as described below, which is crucial for its industrialization. First, the raw materials for the Co/W₅N₄ preparation are cheap (cobalt nitrate (~0.05 \$/g) and ammonium metatungstate (~0.1 \$/g)) and readily available, which is much lower than that of the commercial Pt/C catalyst (~95 \$/g) or its production feedstock, chloroplatinic acid (~60 \$/g). Secondly, the preparation process is relatively simple and facile, requiring only conventional hydrothermal and subsequent heat treatment. The NF in the hydrothermal process can also be bent and folded to obtain larger hydrothermal samples, which will further reduce production cost. In addition, in the production process, organic reagents are not involved, which are harmful to human health and the environment, making it environmentally friendly in general. Obviously, the as-prepared catalyst is considered as a potential HER catalyst because of its many advantages including cost and performance.

4. Conclusion

By using a simple hydrothermal reaction and subsequent high-temperature nitridation treatment, heterostructured Co/W₅N₄ catalysts have been successfully synthesized. The special porous polyhedral morphology of Co/W₅N₄ catalysts greatly increases the exposure of heterostructured interface and active sites. Theoretical calculations reveal a strong d-p hybridization of Co and N at the interface of the Co/W₅N₄, which modulates the d-band center of Co active sites for more favorable H adsorption free energy and further reduces the kinetic barrier of the dissociation of H₂O on W site. Consequently, the Co/W₅N₄ catalyst shows excellent HER activity and durability, surpassing many other reported HER catalysts and the benchmark Pt/C. More importantly, this work confirms the application potential of Co/W₅N₄ material in overall water splitting with alkaline water/seawater media. The synergistic catalytic mechanism facilitated by d-p hybridization may provide profound insights for the design of novel non-precious metal HER electrocatalysts.

CRediT authorship contribution statement

Shipeng Geng: Conceptualization, Methodology, Validation, Formal analysis, Investigation, Writing – original draft. **Liming Chen, Lianmei Kang:** Investigation, Formal analysis. **Ruchun Li:** Investigation, Writing – review & editing. **Haixin Chen, Luo Cheng, and Dandan Cai:** Formal analysis, Visualization. **Yi Wang:** Investigation, Writing – review & editing, Project administration, Funding acquisition. **Shuqin Song:** Supervision, Investigation, Resources, Writing – review & editing, Project administration, Funding acquisition.

Declaration of Competing Interest

The authors declare that they have no known competing financial interests or personal relationships that could have appeared to influence the work reported in this paper.

Data availability

Data will be made available on request.

Acknowledgements

Authors would like to thank the financial support of National Natural Science Foundation of China (21978331, 21975292, 22068008 and 52101186), the Training Program of the Major Research Plan of the National Natural Science Foundation of China (92061124), Guangdong Basic and Applied Basic Research Foundation (2021A1515010167 and 2022A1515011196), Guangzhou Key R&D Program/Plan Unveiled Flagship Project (20220602JBGS02), Guangzhou Basic and Applied Basic Research Project (202201011449), the Research Fund Program of Guangdong Provincial Key Laboratory of Fuel Cell Technology (FC202220, FC202216).

Appendix A. Supporting information

Supplementary data associated with this article can be found in the online version at doi:10.1016/j.apcatb.2023.123486.

References

- [1] X. Zou, Y. Zhang, Noble metal-free hydrogen evolution catalysts for water splitting, *Chem. Soc. Rev.* 44 (2015) 5148–5180, <https://doi.org/10.1039/C4CS00448E>.
- [2] D. Liu, X. Li, S. Chen, H. Yan, C. Wang, C. Wu, Y.A. Haleem, S. Duan, J. Lu, B. Ge, P. M. Ajayan, Y. Luo, J. Jiang, L. Song, Atomically dispersed platinum supported on curved carbon supports for efficient electrocatalytic hydrogen evolution, *Nat. Energy* 4 (2019) 512–518, <https://doi.org/10.1038/s41560-019-0402-6>.
- [3] L. An, C. Wei, M. Lu, H. Liu, Y. Chen, G.G. Scherer, A.C. Fisher, P. Xi, Z.J. Xu, C.-H. Yan, Recent development of oxygen evolution electrocatalysts in acidic environment, *Adv. Mater.* 33 (2021), 2006328, <https://doi.org/10.1002/adma.202006328>.
- [4] Z. Chen, H. Qing, K. Zhou, D. Sun, R. Wu, Metal-organic framework-derived nanocomposites for electrocatalytic hydrogen evolution reaction, *Prog. Mater. Sci.* 108 (2020), 100618, <https://doi.org/10.1016/j.pmatsci.2019.100618>.
- [5] H. Chen, X. Ai, W. Liu, Z. Xie, W. Feng, W. Chen, X. Zou, Promoting subordinate, efficient ruthenium sites with interstitial silicon for Pt-like electrocatalytic activity, *Angew. Chem. Int. Ed.* 131 (2019) 11531–11535, <https://doi.org/10.1002/ange.201906394>.
- [6] Z. He, Y. He, Y. Qiu, Q. Zhao, Z. Wang, X. Kang, L. Yu, L. Wu, Y. Jiang, Monolithic-structured nickel silicide electrocatalyst for bifunctionally efficient overall water splitting, *Appl. Catal. B: Environ.* 342 (2024), 123386, <https://doi.org/10.1016/j.apcatb.2023.123386>.
- [7] X. Wang, X. Han, R. Du, Z. Liang, Y. Zuo, P. Guardia, J. Li, J. Llorca, J. Arbiol, R. Zheng, A. Cabot, Unveiling the role of counter-anions in amorphous transition metal-based oxygen evolution electrocatalysts, *Appl. Catal. B: Environ.* 320 (2023), 121988, <https://doi.org/10.1016/j.apcatb.2022.121988>.
- [8] J. Zhang, G. Chen, Q. Liu, C. Fan, D. Sun, Y. Tang, H. Sun, X. Feng, Competitive adsorption: reducing the poisoning effect of adsorbed hydroxyl on Ru single-atom site with SnO₂ for efficient hydrogen evolution, *Angew. Chem. Int. Ed.* 134 (2022), e202209486, <https://doi.org/10.1002/ange.202209486>.
- [9] Z. Wang, J. Chen, E. Song, N. Wang, J. Dong, X. Zhang, P.M. Ajayan, W. Yao, C. Wang, J. Liu, J. Shen, M. Ye, Manipulation on active electronic states of metastable phase β -NiMoO₄ for large current density hydrogen evolution, *Nat. Commun.* 12 (2021), 5960, <https://doi.org/10.1038/s41467-021-26256-1>.
- [10] X. Zhang, J. Wang, B. Xiao, Y. Pu, Y. Yang, J. Geng, D. Wang, X. Chen, Y. Wei, K. Xiong, Y. Zhu, Resin-based photo-self-Fenton system with intensive mineralization by the synergistic effect of holes and hydroxyl radicals, *Appl. Catal. B: Environ.* 315 (2022), 121525, <https://doi.org/10.1016/j.apcatb.2022.121525>.
- [11] J. Li, L. Li, X. Ma, X. Han, C. Xing, X. Qi, R. He, J. Arbiol, H. Pan, J. Zhao, J. Deng, Y. Zhang, Y. Yang, A. Cabot, Selective ethylene glycol oxidation to formate on nickel selenide with simultaneous evolution of hydrogen, *Adv. Sci.* 10 (2023), 2300841, <https://doi.org/10.1002/advs.202300841>.
- [12] J. Li, L. Li, X. Ma, J. Wang, J. Zhao, Y. Zhang, R. He, Y. Yang, A. Cabot, Y. Zhu, Unraveling the role of iron on Ni-Fe alloy nanoparticles during the electrocatalytic ethanol-to-acetate process, *Nano Res.* (2023), <https://doi.org/10.1007/s12274-023-6049-4>.
- [13] Y. Chen, G. Yu, W. Chen, Y. Liu, G.-D. Li, P. Zhu, Q. Tao, Q. Li, J. Liu, X. Shen, H. Li, X. Huang, D. Wang, T. Asefa, X. Zou, Highly active, nonprecious electrocatalyst comprising borophene subunits for the hydrogen evolution reaction, *J. Am. Chem. Soc.* 139 (2017) 12370–12373, <https://doi.org/10.1021/jacs.7b06337>.
- [14] Y. Luo, L. Tang, U. Khan, Q. Yu, H.-M. Cheng, X. Zou, B. Liu, Morphology and surface chemistry engineering toward pH-universal catalysts for hydrogen evolution at high current density, *Nat. Commun.* 10 (2019), 269, <https://doi.org/10.1038/s41467-018-07792-9>.

[15] F. Zhang, L. Yu, L. Wu, D. Luo, Z. Ren, Rational design of oxygen evolution reaction catalysts for seawater electrolysis, *Trends Chem.* 3 (2021) 485–498, <https://doi.org/10.1016/j.trechm.2021.03.003>.

[16] C. Qian, W. Shao, X. Zhang, X. Mu, X. Gu, M. Yu, L. Ma, S. Liu, S. Mu, Competitive coordination-pairing between Ru clusters and single-atoms for efficient hydrogen evolution reaction in alkaline seawater, *Small* 18 (2022), 2204155, <https://doi.org/10.1002/smll.202204155>.

[17] H. Jin, X. Wang, C. Tang, A. Vasileff, L. Li, A. Slattery, S.-Z. Qiao, Stable and highly efficient hydrogen evolution from seawater enabled by an unsaturated nickel surface nitride, *Adv. Mater.* 33 (2021), 2007508, <https://doi.org/10.1002/adma.202007508>.

[18] L. Wu, L. Yu, B. McElhenney, X. Xing, D. Luo, F. Zhang, J. Bao, S. Chen, Z. Ren, Rational design of core-shell-structured $\text{CoP}_x@\text{FeOOH}$ for efficient seawater electrolysis, *Appl. Catal. B: Environ.* 294 (2021), 120256, <https://doi.org/10.1016/j.apcatb.2021.120256>.

[19] J. Chang, G. Wang, Z. Yang, B. Li, Q. Wang, R. Kuliev, N. Orlovskaya, M. Gu, Y. Du, G. Wang, Y. Yang, Dual-doping and synergism toward high-performance seawater electrolysis, *Adv. Mater.* 33 (2021), 2101425, <https://doi.org/10.1002/adma.202101425>.

[20] L. Yu, Q. Zhu, S. Song, B. McElhenney, D. Wang, C. Wu, Z. Qin, J. Bao, Y. Yu, S. Chen, Z. Ren, Non-noble metal-nitride based electrocatalysts for high-performance alkaline seawater electrolysis, *Nat. Commun.* 10 (2019), 5106, <https://doi.org/10.1038/s41467-019-13092-7>.

[21] L. Wang, Y. Hao, L. Deng, F. Hu, S. Zhao, L. Li, S. Peng, Rapid complete reconfiguration induced actual active species for industrial hydrogen evolution reaction, *Nat. Commun.* 13 (2022), 5785, <https://doi.org/10.1038/s41467-022-33590-5>.

[22] Q. Hu, K. Gao, X. Wang, H. Zheng, J. Cao, L. Mi, Q. Huo, H. Yang, J. Liu, C. He, Subnanometric Ru clusters with upshifted D band center improve performance for alkaline hydrogen evolution reaction, *Nat. Commun.* 13 (2022), 3958, <https://doi.org/10.1038/s41467-022-31660-2>.

[23] X. Zhang, X. Li, Z. Pan, Y. Lai, Y. Lu, Y. Wang, S. Song, Boosting hydrogen evolution electrocatalysis through defect engineering: a strategy of heat and cool shock, *Chem. Eng. J.* 426 (2021), 131524, <https://doi.org/10.1016/j.cej.2021.131524>.

[24] H. Chen, D. Ge, J. Chen, R. Li, X. Zhang, T. Yu, Y. Wang, S. Song, In situ surface reconstruction synthesis of a nickel oxide/nickel heterostructural film for efficient hydrogen evolution reaction, *Chem. Commun.* 56 (2020) 10529–10532, <https://doi.org/10.1039/D0CC03855E>.

[25] H. Yan, C. Tian, L. Wang, A. Wu, M. Meng, L. Zhao, H. Fu, Phosphorus-modified tungsten nitride/reduced graphene oxide as a high-performance, non-noble-metal electrocatalyst for the hydrogen evolution reaction, *Angew. Chem. Int. Ed.* 127 (2015) 6423–6427, <https://doi.org/10.1002/ange.201501419>.

[26] J. Xiong, W. Cai, W. Shi, X. Zhang, J. Li, Z. Yang, L. Feng, H. Cheng, Salt-templated synthesis of defect-rich MoN nanosheets for boosted hydrogen evolution reaction, *J. Mater. Chem. A* 5 (2017) 24193–24198, <https://doi.org/10.1039/C7TA07566A>.

[27] H. Jin, X. Liu, Y. Jiao, A. Vasileff, Y. Zheng, S.-Z. Qiao, Constructing tunable dual active sites on two-dimensional $\text{C}_3\text{N}_4@\text{MoN}$ hybrid for electrocatalytic hydrogen evolution, *Nano Energy* 53 (2018) 690–697, <https://doi.org/10.1016/j.nano.2018.09.046>.

[28] J. Sun, W. Xu, C. Lv, L. Zhang, M. Shakouri, Y. Peng, Q. Wang, X. Yang, D. Yuan, M. Huang, Y. Hu, D. Yang, L. Zhang, Co/MoN hetero-interface nanoflake array with enhanced water dissociation capability achieves the Pt-like hydrogen evolution catalytic performance, *Appl. Catal. B: Environ.* 286 (2021), 119882, <https://doi.org/10.1016/j.apcatb.2021.119882>.

[29] J. Wang, W. Chen, T. Wang, N. Bate, C. Wang, E. Wang, A strategy for highly dispersed Mo₂C/MoN hybrid nitrogen-doped graphene via ion-exchange resin synthesis for efficient electrocatalytic hydrogen reduction, *Nano Res.* 11 (2018) 4535–4548, <https://doi.org/10.1007/s12274-018-2034-8>.

[30] J. Zheng, J. Chen, L. Xiao, X. Cheng, H. Cui, In situ integrated $\text{Co}_3\text{W}-\text{WN}$ hybrid nanostructure as an efficient bifunctional electrocatalyst by accelerating water dissociation and enhancing oxygen evolution, *ChemElectroChem* 7 (2020) 4971–4978, <https://doi.org/10.1002/celec.202001454>.

[31] Y. Zhou, B. Chu, Z. Sun, L. Dong, F. Wang, B. Li, M. Fan, Z. Chen, Surface reconstruction and charge distribution enabling Ni/W₃N₄ Mott-Schottky heterojunction bifunctional electrocatalyst for efficient urea-assisted water electrolysis at a large current density, *Appl. Catal. B: Environ.* 323 (2023), 122168, <https://doi.org/10.1016/j.apcatb.2022.122168>.

[32] R. Yang, Y. Zhou, Y. Xing, D. Li, D. Jiang, M. Chen, W. Shi, S. Yuan, Synergistic coupling of CoFe-LDH arrays with NiFe-LDH nanosheet for highly efficient overall water splitting in alkaline media, *Appl. Catal. B: Environ.* 253 (2019) 131–139, <https://doi.org/10.1016/j.apcatb.2019.04.054>.

[33] G. Kresse, J. Furthmüller, Efficient iterative schemes for ab initio total-energy calculations using a plane-wave basis set, *Phys. Rev. B* 54 (1996) 11169–11186, <https://doi.org/10.1103/PhysRevB.54.11169>.

[34] P.E. Blöchl, Projector augmented-wave method, *Phys. Rev. B* 50 (1994) 17953–17979, <https://doi.org/10.1103/PhysRevB.50.17953>.

[35] J.P. Perdew, K. Burke, M. Ernzerhof, Generalized gradient approximation made simple, *Phys. Rev. Lett.* 77 (1996) 3865–3868, <https://doi.org/10.1103/PhysRevLett.77.3865>.

[36] G. Henkelman, B.P. Uberuaga, H. Jónsson, A climbing image nudged elastic band method for finding saddle points and minimum energy paths, *J. Chem. Phys.* 113 (2000) 9901–9904, <https://doi.org/10.1063/1.1329672>.

[37] H. Dong, W. Li, Y. Ou, D. Gao, Y. Yang, Y. Zhang, P. Xiao, Self-assembly hydrothermal synthesis of silverton-type polyoxometalate-based photocatalysts for enhanced degradation, *Langmuir* 36 (2020) 4454–4464, <https://doi.org/10.1021/acs.langmuir.9b03721>.

[38] Y. Gu, A. Wu, Y. Jiao, H. Zheng, X. Wang, Y. Xie, L. Wang, C. Tian, H. Fu, Two-dimensional porous molybdenum phosphide/nitride heterojunction nanosheets for pH-universal hydrogen evolution reaction, *Angew. Chem. Int. Ed.* 60 (2021) 6673–6681, <https://doi.org/10.1002/anie.202016102>.

[39] X. Wu, S. Zhou, Z. Wang, J. Liu, W. Pei, P. Yang, J. Zhao, J. Qiu, Engineering multifunctional collaborative catalytic interface enabling efficient hydrogen evolution in all pH range and seawater, *Adv. Energy Mater.* 9 (2019), 1901333, <https://doi.org/10.1002/aenm.201901333>.

[40] Y. Yang, L. Dang, M.J. Shearer, H. Sheng, W. Li, J. Chen, P. Xiao, Y. Zhang, R. J. Hamers, S. Jin, Highly active trimetallic NiFeCr layered double hydroxide electrocatalysts for oxygen evolution reaction, *Adv. Energy Mater.* 8 (2018), 1703189, <https://doi.org/10.1002/aenm.201703189>.

[41] C.-T. Dinh, A. Jain, F.P.G. de Arquer, P. De Luna, J. Li, N. Wang, X. Zheng, J. Cai, B. Z. Gregory, O. Voznyy, B. Zhang, M. Liu, D. Sinton, E.J. Crumlin, E.H. Sargent, Multi-site electrocatalysts for hydrogen evolution in neutral media by destabilization of water molecules, *Nat. Energy* 4 (2019) 107–114, <https://doi.org/10.1038/s41560-018-0296-8>.

[42] B. Zhang, L. Zhang, Q. Tan, J. Wang, J. Liu, H. Wan, L. Miao, J. Jiang, Simultaneous interfacial chemistry and inner Helmholtz plane regulation for superior alkaline hydrogen evolution, *Energ. Environ. Sci.* 13 (2020) 3007–3013, <https://doi.org/10.1039/D0EE02020F>.

[43] X. Li, X. Yang, L. Liu, H. Zhao, Y. Li, H. Zhu, Y. Chen, S. Guo, Y. Liu, Q. Tan, G. Wu, Chemical vapor deposition for N/S-doped single fe site catalysts for the oxygen reduction in direct methanol cells, *ACS Catal.* 11 (2021) 7450–7459, <https://doi.org/10.1021/acscatal.0c05446>.

[44] L. Wu, L. Su, Q. Liang, W. Zhang, Y. Men, W. Luo, Boosting hydrogen oxidation kinetics by promoting interfacial water adsorption on d-p hybridized Ru catalysts, *ACS Catal.* 13 (2023) 4127–4133, <https://doi.org/10.1021/acscatal.2c05547>.

[45] H. Yan, Y. Xie, Y. Jiao, A. Wu, C. Tian, X. Zhang, L. Wang, H. Fu, Holey reduced graphene oxide coupled with an Mo₂N–Mo₂C heterojunction for efficient hydrogen evolution, *Adv. Mater.* 30 (2018), 1704156, <https://doi.org/10.1002/adma.201704156>.

[46] Y. Wang, B. Zhu, B. Cheng, W. Macay, P. Kuang, J. Yu, Hollow carbon sphere-supported Pt/Co₃O₄ hybrid with excellent hydrogen evolution activity and stability in acidic environment, *Appl. Catal. B: Environ.* 314 (2022), 121503, <https://doi.org/10.1016/j.apcatb.2022.121503>.

[47] L. Chen, L. Kang, D. Cai, S. Geng, Y. Liu, J. Chen, S. Song, Y. Wang, Ultrafine Pt-based catalyst decorated with oxytrogenophilic ni-sites accelerating alkaline H₂O dissociation for efficient hydrogen evolution, *J. Colloid Interf. Sci.* (2023), <https://doi.org/10.1016/j.jcis.2023.07.119>.

[48] T. Ma, H. Cao, S. Li, S. Cao, Z. Zhao, Z. Wu, R. Yan, C. Yang, Y. Wang, P.A. van Aken, L. Qiu, Y.-G. Wang, C. Cheng, Crystalline lattice-confined atomic Pt in metal carbides to match electronic structures and hydrogen evolution behaviors of platinum, *Adv. Mater.* 34 (2022), 2206368, <https://doi.org/10.1002/adma.202206368>.

[49] M. Ning, L. Wu, F. Zhang, D. Wang, S. Song, T. Tong, J. Bao, S. Chen, L. Yu, Z. Ren, One-step spontaneous growth of NiFe layered double hydroxide at room temperature for seawater oxygen evolution, *Mater. Today Phys.* 19 (2021), 100419, <https://doi.org/10.1016/j.mtphys.2021.100419>.

[50] M. Xiao, C. Wu, J. Zhu, C. Zhang, Y. Li, J. Lyu, W. Zeng, H. Li, L. Chen, S. Mu, In situ generated layered NiFe-LDH/MOF heterostructure nanosheet arrays with abundant defects for efficient alkaline and seawater oxidation, *Nano Res.* (2023), <https://doi.org/10.1007/s12274-023-5608-z>.